CHIN. PHYS. LETT. Vol. 38, No. 12 (2021) 127401

Structures and Physical Properties of V-Based Kagome Metals CsV_6Sb_6 and CsV_8Sb_{12}

Qiangwei Yin(殷蔷薇), Zhijun Tu(涂志俊), Chunsheng Gong(龚春生), Shangjie Tian(田尚杰), and Hechang Lei(雷和畅)*

Department of Physics and Beijing Key Laboratory of Opto-electronic Functional Materials & Micro-nano Devices, Renmin University of China, Beijing 100872, China

(Received 22 October 2021; accepted 2 November 2021; published online 12 November 2021)

We report two new members of V-based kagome metals CsV_6Sb_6 and CsV_8Sb_{12}. The most striking structural feature of CsV_6Sb_6 is the V kagome bilayers. For CsV_8Sb_{12}, there is an intergrowth of two-dimensional V kagome layers and one-dimensional V chains, and the latter ones lead to the orthorhombic symmetry of this material. Further measurements indicate that these two materials exhibit metallic and Pauli paramagnetic behaviors. More importantly, different from CsV_3Sb_5, the charge density wave state and superconductivity do not emerge in CsV_6Sb_6 and CsV_8Sb_{12} when temperature is above 2 K. Small magnetoresistance with saturation behavior and linear field dependence of Hall resistivity at high field and low temperature suggest that the carriers in both materials should be uncompensated with much different concentrations. The discovery of these two new V-based kagome metals sheds light on the exploration of correlated topological materials based on kagome lattice.

DOI: 10.1088/0256-307X/38/12/127401

Two-dimensional (2D) kagome lattice is a paradigm to study the effects of strongly geometrical frustration which could host many exotic magnetic ground states like quantum spin liquid state with fractionalized excitations.[1,2] When introducing charge degrees of freedom, Janus-like kagome lattice exhibits nontrivial topological electronic structures with unusual features of Dirac nodal points, flat band and saddle point.[3–6] More importantly, the combination of magnetic correlation and band topology leads to the emergence of various of exotic correlated topological phenomena in metallic materials with kagome lattice (kagome metals), such as large anomalous Hall effect (AHE),[3,7–9] negative magnetism of flat band,[10] large magnetic-field tunability[11] and the formation of Chern gap with edge state.[12]

Very recently, the kagome metals with electron correlations other than magnetic ones have been extended to the V-based materials AV_3Sb_5 (A = K, Rb and Cs), and they exhibit the coexistence of charge density wave (CDW) state and superconductivity with a nonzero Z_2 topological invariant.[13–16] Such phenomena are closely related to the physics of van Hove filling in kagome lattice.[17–19] Moreover, the CDW state with three-dimensional (3D) $2\times2\times2$ superlattice[20,21] shows some exotic behaviors. For instance, the CDW state may have a chirality which could result in large anomalous Hall conductivity without long-range ferromagnetism.[22–25] In addition, there is an intricate relationship between CDW state and superconductivity. For example, when the CDW transition is suppressed with pressure monotonically, the superconductivity shows an unusual multiple-dome feature with a significant enhancement.[26–30] The roton pair density wave state has also been observed in the superconducting state.[31]

In order to understand these diverse properties of V-based kagome metals further, not only the comprehensive studies on AV_3Sb_5 but also the exploration of novel V-based kagome materials is important. For many of magnetic kagome metals, a series of compounds with the key kagome layer exist, such as the binary T_mX_n kagome metals (T = Mn, Fe, Co; X = Sn, Ge; $m:n$ = 3 : 1, 3 : 2, 1 : 1).[6] Systematic studies on these materials can provide some important clues to understand the effects of different local structural environment and strength of interlayer coupling on the properties of kagome layer. But such kind of homologous compounds is still scarce in V-based kagome materials. In this work, we report the discovery of V-based kagome metals CsV_6Sb_6 and CsV_8Sb_{12}, two homologous compounds of CsV_3Sb_5. The characterizations of physical properties of single crystals indicate that these compounds show metallic behaviors

Supported by the National Key R&D Program of China (Grant No. 2018YFE0202600), the Beijing Natural Science Foundation (Grant No. Z200005), the National Natural Science Foundation of China (Grant Nos. 11822412 and 11774423), the Fundamental Research Funds for the Central Universities and Research Funds of Renmin University of China (RUC) (Grant Nos. 19XNLG17 and 20XNH062), the Outstanding Innovative Talents Cultivation Funded Programs 2020 of Renmin Univertity of China, the Beijing National Laboratory for Condensed Matter Physics, and Collaborative Research Project of Laboratory for Materials and Structures, Institute of Innovative Research, Tokyo Institute of Technology.

*Corresponding author. Email: hlei@ruc.edu.cn

© 2021 Chinese Physical Society and IOP Publishing Ltd

without CDW and superconducting transitions down to 2 K.

Methods. Single crystals of CsV_6Sb_6 and CsV_8Sb_{12} were grown using self-flux method. High-purity Cs (ingot), V (powder) and Sb (grain) were taken in a stoichiometric molar ratio of 1 : 6 : 30 for CsV_6Sb_6 and 1 : 8 : 50 for CsV_8Sb_{12}, respectively, and placed in a quartz tube with alumina crucible under partial argon atmosphere. The sealed quartz tubes for both materials were heated up to 1373 K for 12 h and soaked there for another 24 h. After that, for CsV_6Sb_6, the temperature was rapidly cooled down to 1273 K with subsequently cooling down to 1163 K at 1.5 K/h, and then the temperature was held there for 70 h. For CsV_8Sb_{12}, the temperature was cooled down directly to 1123 K with the rate of 2 K/h. Finally, the ampoules were taken out of furnace and the single crystals were separated from the flux by a centrifuge. Shiny crystals with typical sizes of $1 \times 1 \times 0.02\,mm^3$ (length × width × thickness) for CsV_6Sb_6 and $4 \times 1 \times 0.1\,mm^3$ for CsV_8Sb_{12} can be obtained. Both crystals are stable in air. In order to prevent the reaction of Cs with air and water, all the preparation processes except the sealing and heat treatment procedures are carried out in an argon-filled glove box. The elemental analysis was performed using the energy-dispersive x-ray spectroscopy (EDX). XRD patterns were collected using a Bruker D8 x-ray diffractometer with Cu K_α radiation ($\lambda = 1.5418$ Å) at room temperature. Single crystal XRD patterns at 300 K were collected using a Bruker D8 VENTURE PHOTO Ⅱ diffractometer with multilayer mirror monochromatized Mo K_α ($\lambda = 0.71073$ Å) radiation. Unit cell refinement and data merging were carried out with the SAINT program, and an absorption correction was applied using Multi-Scans. The structural solutions were obtained by intrinsic phasing methods using the program APEX3,[32] and the final refinement was completed with the SHELXL suite of programs.[33] Electrical transport measurements were carried out in a Quantum Design physical property measurement system (PPMS-14T). The field dependences of *ab*-plane longitudinal and transverse electrical resistivity were measured using a five-probe method and the current flows in the *ab* plane of the crystal. The magnetoresistance and Hall resistivity were obtained from symmetrizing and antisymmetrizing the longitudinal and transverse resistivity measured at the positive and negative fields, respectively. The *c*-axis resistivity was measured by attaching current and voltage wires on the opposite sides of the plate-like crystal. Magnetization measurements were performed in a Quantum Design magnetic property measurement system (MPMS3).

Results and Discussion. As shown in Fig. 1(a), CsV_3Sb_5 has a layered structure with hexagonal symmetry (space group $P6/mmm$, No. 191), with the *a*- and *c*-axial lattice parameters being 5.5055 Å and 9.3287 Å.[13] It consists of Cs, Sb and V–Sb layer stacking along *c* axis alternatively [Fig. 1(a)].[13] For the Cs layer, Cs atoms form a perfect triangle lattice with the distance of Cs atoms $d_{Cs-Cs} = 5.5055$ Å [Fig. 2(a)]. For the Sb layer, Sb atoms compose a honeycomb lattice with $d_{Sb-Sb} = 3.1786$ Å and Cs atoms are located at the centers of each hexagons [Fig. 2(a)]. Because there are two Sb atoms in one unit cell, this layer is denoted by the Sb_2 layer. The key structural ingredient of CsV_3Sb_5 is the 2D undistorted V kagome lattice in the V–Sb layer and the distance of V atoms $d_{V-V} = 2.7528$ Å [Fig. 2(b)]. The Sb atoms occupy at the centers of V hexagons with $d_{V-Sb} = 2.7528$ Å when Sb atoms in the Sb_2 layer are located below and above the centers of V triangles [Fig. 1(d)]. This V–Sb layer can be denoted by V_3Sb layer due to three V and one Sb atoms in one unit cell. Because there are one Cs, two Sb_2 and one V_3Sb layers in each unit cell, the chemical formula of CsV_3Sb_5 can be expressed as $CsV_3Sb_5 = Cs + 2Sb_2 + V_3Sb$.

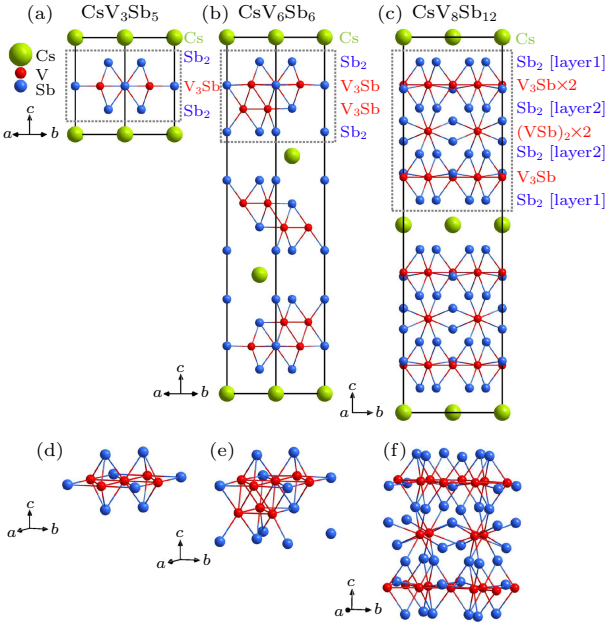

Fig. 1. Front view of structures of (a) CsV_3Sb_5, (b) CsV_6Sb_6, and (c) CsV_8Sb_{12}. The big green, small red and medium blue balls represent Cs, V, and Sb atoms. The black lines represent the unit cell edges. (d)–(f) Side view of V–Sb building blocks emphasized by dotted rectangles in (a)–(c).

For layered CsV_6Sb_6, it has a similar hexagonal structural symmetry to CsV_3Sb_5 (space group $R\bar{3}m$, No. 166) with $a = 5.5575(8)$ Å and $c = 35.165(9)$ Å (Table 1). The structures of Cs layer and Sb_2 layer with Sb1 and Sb2 sites in CsV_6Sb_6 are also similar to those in CsV_3Sb_5, and the former has slightly larger d_{Cs-Cs} (= 5.5055 Å) and d_{Sb-Sb} (= 3.2086 Å) [Figs. 1(b) and 2(c)]. Instead of the V_3Sb monolayers

in CsV_3Sb_5, there are $2V_3Sb$ bilayers with V and Sb1 sites in CsV_6Sb_6 [Figs. 1(b) and 2(d)], similar to that in Fe_3Sn_2.[34] The shift of top V_3Sb layer along the direction of $\frac{1}{3}a$–$\frac{1}{3}b$ will coincide with the bottom one. Due to this shift, the Sb atoms in one layer are located below and above the centers of V triangles in another layer when another half of V triangles in both layers form the distorted octahedra of V atoms [Figs. 1(e) and 2(d)]. Such inequivalent local environments of V triangles also lead to the distortion of kagome layers with two kinds of equilateral triangles which have different intralayer V–V distances $d^{\text{intra}}_{\text{V-V}} = 2.7826$ Å (green ones) and 2.7749 Å (red ones). The former one with smaller value could be ascribed to the stronger V–V interactions in the V octahedra. Because of this distortion, the intralayer V–Sb distance $d^{\text{intra}}_{\text{V-Sb}}$ (= 2.7794 Å) falls in between two values of $d^{\text{intra}}_{\text{V-V}}$. In contrast, the interlayer V–V and V–Sb distances ($d^{\text{inter}}_{\text{V-V}} = 2.8937$ Å and $d^{\text{inter}}_{\text{V-Sb}} = 2.8452$ Å) are much larger than those of $d^{\text{intra}}_{\text{V-V}}$ and $d^{\text{intra}}_{\text{V-Sb}}$, reflecting the relatively weak interlayer interaction when compared to the intralayer one. It must be noted that the Sb atoms in the kagome layer are slightly moved along the c axis and toward to the center of bilayer (see the different z values of V and Sb1 in Table 2). Since there are three Cs, six Sb_2 and three V_3Sb bilayers in one unit cell, we have $3CsV_6Sb_6 = 3Cs + 6Sb_2 + 3\times 2V_3Sb$.

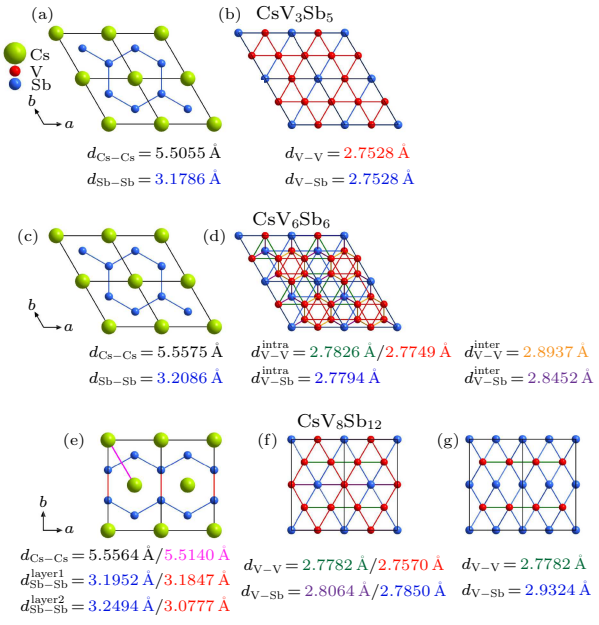

Fig. 2. Top view of (a) Cs, Sb_2 layers and (b) V_3Sb layer of CsV_3Sb_5. (c) Cs, Sb_2 layers and (d) $2V_3Sb$ bilayer of CsV_6Sb_6. (e) Cs, Sb_2 layers, (f) V_3Sb layer, and (g) $(VSb)_2$ layer of CsV_8Sb_{12}. The corresponding Cs–Cs, Sb–Sb, V–V, V–Sb atomic distances in each layer are shown below the figures.

Table 1. Crystallographic data of CsV_6Sb_6 and CsV_8Sb_{12} at 300 K.

Chemical formula	CsV_6Sb_6	CsV_8Sb_{12}
Space group	$R\bar{3}m$	$Fmmm$
Crystal system	Rhombohedral	Orthorhombic
a (Å)	5.5575(8)	5.5564(3)
b (Å)	5.5575(8)	9.5260(5)
c (Å)	35.165(9)	36.227(2)
V (Å^3)	940.59(36)	1917.50(18)
Z	3	4
Dimensions (mm^3) (min/mid/max)	0.05/0.40/0.50	0.10/0.36/0.39
Calculated density (g/cm^3)	6.047	6.880
Absolute coefficient (mm^{-1})	19.270	21.971
h	$-7 \le h \le 7$	$-7 \le h \le 6$
k	$-6 \le k \le 6$	$-12 \le k \le 11$
l	$-46 \le l \le 46$	-46 x$\le l \le 48$
Reflections (collected/unique/R indices)	2536/334/0.0642	5846/709/0.0697
Data/parameters/restraints	334/18/0	709/36/0
GOF on F^2	1.139	1.139
R indices (all data) ($R1/wR2$)[a]	0.0825/0.2643	0.0590/0.1824

[a] $R1 = \sum |F_0| - |F_c| / \sum |F_0|$, $wR2 = [\sum(|F_0^2 - F_c^2|)^2 / \sum(wF_0^2)^2]^{1/2}$.

CsV_8Sb_{12} has an orthorhombic symmetry (space group $Fmmm$, No. 69) with $a = 5.5564(3)$ Å, $b = 9.5260(5)$ Å, and $c = 36.227(2)$ Å (Table 1). Although the structure of CsV_8Sb_{12} is much more complicated than CsV_3Sb_5 and CsV_6Sb_6, these three materials still share some common structure features. The local environments of Cs layer, Sb_2 layer with Sb2 and Sb3 sites and V_3Sb layer with V1, V2, and Sb1 sites in CsV_8Sb_{12} [Figs. 1(c), 2(e) and 2(f)] are similar to those in CsV_3Sb_5 and CsV_6Sb_6. However, they are compressed along the b axis of orthorhombic lattice (the [210] direction in hexagonal lattice) and it leads to the distortions of these layers with inequivalent intralayer atomic distances, such as $d_{\text{Cs-Cs}} = 5.5564/5.5140$ Å, $d_{\text{V-V}} = 2.7782/2.7570$ Å, and $d_{\text{V-Sb}} = 2.8064/2.7850$ Å [Figs. 2(e) and 2(f)]. In addition, such compression also results in the significant movement of Sb atoms in the kagome layer

along the c axis [Figs. 1(c) and 1(f) as well as Table 2]. Correspondingly, the $d_{\mathrm{Sb-Sb}}$ in both Sb_2 layers above and below the V kagome layer [labeled as Sb_2 layer 1 and layer 2 in Fig. 1(c)] become different. The $d_{\mathrm{Sb-Sb}}$ in Sb_2 layer 1 are 3.1952 Å and 3.1847 Å when those in Sb_2 layer 2 are 3.2494 Å and 3.0777 Å [Fig. 2(e)]. The most distinctive structural feature of CsV_8Sb_{12} is the $(VSb)_2$ layer with V3 and Sb4 sites between two V_3Sb kagome layers [Figs. 1(c) and 2(g)]. In this layer, there are two Sb layers located below and above a V layer with $d_{\mathrm{V-Sb}} = 2.9324$ Å. For the former one, the in-plane arrangement of Sb atoms is similar to that in the V_3Sb layer [Fig. 1(f)]. For the latter one, V atoms form one-dimensional (1D) chains along the a direction with $d_{\mathrm{V-V}} = 2.7782$ Å [Figs. 1(f) and 2(g)], which is exactly the same as the value of $d_{\mathrm{V-V}}$ in the V_3Sb layer along the a axis. Actually, such 1D chains of V atoms should lead to the orthorhombic symmetry of CsV_8Sb_{12}. There are two Cs, eight Sb_2, four V_3Sb, and two VSb_2 layers in one unit cell and each layer contains twice atoms when compared to CsV_3Sb_5 and CsV_6Sb_6, thus we have $4CsV_8Sb_{12} = 2\times[2Cs + 8Sb_2 + 4\,V_3Sb + 2(VSb)_2]$.

Table 2. Atomic positions, site occupation factor (s.o.f.) and equivalent isotropic displacement parameters U_{eq} obtained from the XRD fits for CsV_6Sb_6 and CsV_8Sb_{12} at 300 K.

CsV_6Sb_6						
Atom	Site	x/a	y/b	z/c	s.o.f.	U_{eq} (Å^2)
Cs	3a	2/3	1/3	1/3	1	0.0390(11)
V	18h	0.6662(4)	83331(2)	0.20093(7)	1	0.0146(10)
Sb1	6c	2/3	1/3	0.19918(5)	0.9548	0.0148(9)
Sb2	6c	1/3	2/3	0.26503(5)	0.9685	0.0177(8)
Sb3	6c	0	0	0.26505(6)	0.9646	0.0183(9)
CsV_8Sb_{12}						
Atom	Site	x/a	y/b	z/c	s.o.f.	U_{eq} (Å^2)
Cs	4a	1/2	0	1/2	1	0.0239(6)
V1	8i	1/2	1/2	0.37349(10)	0.9719	0.0041(7)
V2	16j	1/4	3/4	0.37340(7)	0.9831	0.0068(6)
V3	8f	1/4	1/4	1/4	0.9410	0.0089(8)
Sb1	8i	0	1/2	0.36253(4)	0.9869	0.0077(4)
Sb2	16m	1/2	0.66716(10)	0.43449(3)	1	0.0094(4)
Sb3	16m	1/2	0.33846(9)	0.31147(3)	1	0.0078(4)
Sb4	8i	0	0	0.22243(4)	1	0.0086(4)

For CsV_6Sb_6, the fit of single crystal XRD with floating site occupation factor (s.o.f) gives that the ratio of three elements is close to 1 : 6 : 5.78, possibly with a very small amount of Sb vacancies on all of three Sb sites (Table 2). But the average atomic ratios of Cs : V : Sb obtained from the EDX measurement is 1 : 6.02(7) : 6.22(8) when setting the content of Cs as 1, i.e., there are no Sb vacancies. Thus, within the error range, the CsV_6Sb_6 should be a stoichiometric compound. In contrast, for CsV_8Sb_{12}, similar fit of XRD pattern shows that there are vacancies in both V and Sb sites, especially for the V on the 1D chain (V3 site in Table 2). The atomic ratio of Cs : V : Sb is 1 : 7.76 : 11.98. The EDX result also indicates that the significant V deficiencies exist in this material (Cs : V : Sb = 1 : 7.00(2) : 11.38(8) when setting the content of Cs as 1).

Figures 3(a) and 3(b) show the XRD pattern of CsV_6Sb_6 and CsV_8Sb_{12} single crystals, respectively. All the peaks can be indexed by the indices of (00l) lattice planes. They indicate that the crystal surfaces are parallel to the ab-plane and perpendicular to the c-axis for both the materials. The insets in Fig. 3(a) and 3(b) show the photographs of typical CsV_6Sb_6 and CsV_8Sb_{12} crystals on a 1 mm grid paper. It can be seen that the shapes of these two crystals are quite different. For the CsV_6Sb_6 crystal, it has a hexagonal thin-plate-like shape [inset of Fig. 3(a)], consistent with the layered structure and its rhombohedral symmetry. In contrast, for the CsV_8Sb_{12} crystal, it has a rectangular shape with relatively large thickness. This reflects the orthorhombic distortion of kagome lattice.

Figure 3(c) presents temperature dependence of the zero-field a-axis resistivity $\rho_{\mathrm{aa}}(T)$ for CsV_6Sb_6 and CsV_8Sb_{12} single crystals. Both of $\rho_{\mathrm{aa}}(T)$ curves exhibit similarly decreasing trend with lowering temperature. It clearly indicates that both materials are metals. In addition, the residual resistivity ratio, defined as $\rho_{\mathrm{aa}}(300\,\mathrm{K})/\rho_{\mathrm{aa}}(2\,\mathrm{K})$, is about 1.94 for CsV_6Sb_6 when compared to the value of 2.8 for CsV_8Sb_{12}. It must be noted that distinctly different from AV_3Sb_5, the resistivity curves do not show any anomalies in the whole temperature range (2–300 K). Moreover, as shown in Fig. 3(d), again, there are no transitions in the magnetic susceptibility $\chi(T)$ curves at $\mu_0 H = 1$ T with zero-field-cooling (ZFC) mode for $H \| c$. These results indicate that the CDW and superconducting transitions are absent in both CsV_6Sb_6 and CsV_8Sb_{12}

when T is above 2 K. The $\chi(T)$ curves of both materials exhibit weak temperature dependence at $T > 50$ K with very small values. Such a kind of Pauli paramagnetism is consistent with the itinerant features of electrons in CsV_6Sb_6 and CsV_8Sb_{12} and suggests that the V ions in these materials do not have obvious local moment. The slight upturns of $\chi(T)$ curves in low temperature region could be due to the trace amount of impurities on the surface of crystals.

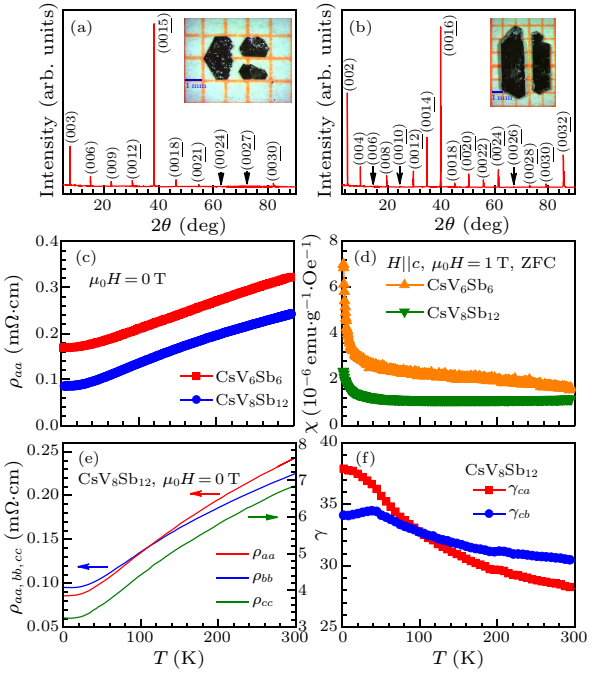

Fig. 3. [(a), (b)] XRD pattern of a CsV_6Sb_6 and CsV_8Sb_{12} single crystal, respectively. Insets: photos of typical CsV_6Sb_6 and CsV_8Sb_{12} single crystals on a 1 mm grid paper. (c) Temperature dependence of a-axis resistivity $\rho_{aa}(T)$ at zero field for CsV_6Sb_6 and CsV_8Sb_{12} single crystals. (d) The $\chi(T)$ as a function of temperature when $H\|c$ and $\mu_0 H = 1$ T with ZFC mode for both the materials. (e) Temperature dependence of $\rho(T)$ along three crystallographic axes of CsV_8Sb_{12}. (f) Temperature dependence of anisotropy of resistivity $\gamma_{ca}(T) = \rho_{cc}(T)/\rho_{aa}(T)$ and $\gamma_{cb}(T) = \rho_{cc}(T)/\rho_{bb}(T)$ for CsV_8Sb_{12}.

For CsV_8Sb_{12}, the out-of-plane resistivity ρ_{cc} is much larger than those in-plane ones (ρ_{aa} and ρ_{bb}) [Fig. 3(e)], which is reflected in the large anisotropy of resistivity $\gamma_{ca} = \rho_{cc}/\rho_{aa}$ and $\gamma_{cb} = \rho_{cc}/\rho_{bb}$ [Fig. 3(f)]. The values of γ_{ca} and γ_{cb} are about 28 and 30 at 300 K, and increase to 38 and 34 at 2 K. Notably, these γ values are larger than those of CsV_3Sb_5 ($\gamma \sim 10$ at 300 K and 23 at 8 K),[35] suggesting a weaker interlayer coupling in CsV_8Sb_{12}, i.e., the two-dimensionality is more obvious. On the other hand, the comparable γ_{ca} and γ_{cb} imply the small in-plane anisotropy of CsV_8Sb_{12} even it has an orthorhombic structure. The slightly smaller ρ_{aa} than ρ_{bb} at low temperature could be due to the existent of V chains along the a-axis, in which the intrachain hopping could enhance conductivity.

CsV_6Sb_6 and CsV_8Sb_{12} exhibit the similar behavior of magnetoresistance ($MR = [\rho_{xx}(T, \mu_0 H) - \rho_{xx}(T, 0)]/\rho_{xx}(T, 0)$) for $H\|c$ and $I\|a$. At low temperature, the MR increases with field gradually and then saturates at high field [Figs. 4(a) and 4(c)]. The values at 2 K and 9 T are about 11% and 35% for CsV_6Sb_6 and CsV_8Sb_{12}. These saturation behaviors of MR with relatively small high-field values are remarkably different from the unsaturated MR even at very high field with extremely large absolute values in the well-known compensated semimetals, like WTe_2 and LaBi.[36,37] In the framework of two-band model, it implies that one type of carriers has a much higher concentration than the other type.[38] With increasing temperature, the saturation value of MR becomes smaller and the saturation field shifts to higher field. At even higher temperatures, the saturation behavior can not be observed at $\mu_0 H \leq 9$ T and the MR exhibits a quasi-linear behavior. This evolution of MR can be partially explained by the decrease of carrier mobility μ at high temperature.[38]

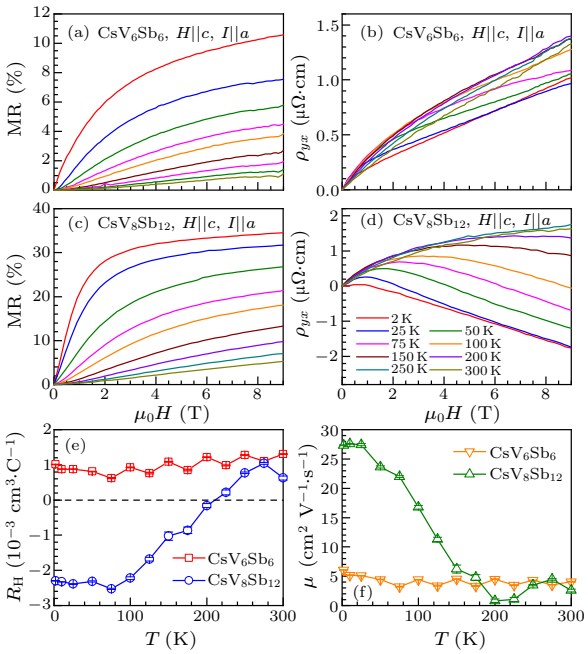

Fig. 4. Field dependences of [(a), (c)] MR and [(b), (d)] Hall resistivity $\rho_{yx}(\mu_0 H)$ up to $\mu_0 H = 9$ T with $H\|c$ and $I\|a$ at various temperatures for CsV_6Sb_6 and CsV_8Sb_{12}. The color codes in (a)–(d) are the same. (e) Temperature dependences of $R_H(T)$ derived from the linear fit of $\rho_{yx}(\mu_0 H)$ curve at high-field region. (f) Derived $\mu(T)$ as a function of temperature.

As shown in Fig. 4(b), the Hall resistivity $\rho_{yx}(\mu_0 H)$ of CsV_6Sb_6 shows a convex shape in low-field region and changes to a nearly linear behavior in high-field region. Moreover, the slopes of $\rho_{yx}(\mu_0 H)$ curves in the whole temperature range are positive. In contrast, the $\rho_{yx}(\mu_0 H)$ curves of CsV_8Sb_{12} at high fields and low temperatures exhibit linear behaviors with negative slopes. These results suggest that the dominant carriers are holes and electrons in CsV_6Sb_6

and CsV_8Sb_{12}, respectively. Moreover, different from CsV_6Sb_6, the low-temperature $\rho_{yx}(\mu_0 H)$ curve of CsV_8Sb_{12} has a maximum value. It shifts to higher fields with increasing temperature and the corresponding field H_m is larger than 9 T when $T > 200$ K. The Hall coefficient $R_{\rm H}(T) \equiv \rho_{yx}(\mu_0 H)/\mu_0 H$ determined from the linear fits of $\rho_{yx}(\mu_0 H, T)$ curves in high-field region. For CsV_6Sb_6, the $R_{\rm H}(T)$ shows a weak temperature dependence [Fig. 4(e)]. However, the $R_{\rm H}(T)$ of CsV_8Sb_{12} is almost unchanged when $T \leq 75$ K and then increases at higher temperature with changing the sign from negative to positive at 225 K. Because of the saturation behavior of MR, this temperature dependence and sign change of $R_{\rm H}(T)$ should not be ascribed to the type change of dominant carriers at high temperature but be explained by the shift of low-field part of $R_{\rm H}$ with $H < H_m$ to 9 T. For this region, carrier mobility μ has a significant influence on $R_{\rm H}$ according to the two-band model.[39] At 2 K, we evaluate the apparent carrier concentration $n_{\rm a}$ using the formula $|R_{\rm H}| = 1/|e|n_{\rm a}$ and it is $6.18(1) \times 10^{21}$ cm^{-3} and $2.718(8) \times 10^{21}$ cm^{-3} for CsV_6Sb_6 and CsV_8Sb_{12}, respectively. In addition, according to the single-band model, the value of μ can be calculated using the formula $\mu = \sigma_{xx}(0)/|e|n_{\rm a} \approx 1/|e|n_{\rm a}\rho_{xx}(0) = R_{\rm H}/\rho_{xx}(0)$. The temperature dependences of derived $\mu(T)$ for both the compounds are presented in Fig. 4(f). For CsV_6Sb_6, the $\mu(T)$ is small ($6.07(1)$ cm$^2\cdot$V$^{-1}\cdot$s^{-1} at 2 K) and insensitive to temperature, implying that the dominant scattering mechanism may be the electron-impurity scattering. In contrast, for CsV_8Sb_{12}, the $\mu(T)$ increases with decreasing temperature in general and reaches $27.32(8)$ cm$^2\cdot$V$^{-1}\cdot$s^{-1} at 2 K. It suggests that the electron-phonon scattering mechanism should be the dominant and the decreased scatting rate because of the gradually frozen phonons at low temperature enhances $\mu(T)$.[39] It should be noted that the values of $n_{\rm a}$ and μ for both CsV_6Sb_6 and CsV_8Sb_{12} are lower than those in CsV_3Sb_5,[23] explaining well their much larger low-temperature resistivity than the latter.[23] Moreover, the drastic changes of $n_{\rm a}$ and μ of CsV_6Sb_6 and CsV_8Sb_{12} when compared with CsV_3Sb_5 reflect their obviously different electronic structures and Fermi surfaces near Fermi energy level $E_{\rm F}$, originating from their different structures. These changes also explain the absence of CDW and superconductivity in the former materials partially because the $E_{\rm F}$ may have moved away from the van Hove singularity near the M point of Brillouin zone.

In summary, single crystals of two new members of V-based kagome metals CsV_6Sb_6 and CsV_8Sb_{12} have been grown successfully. Transport and magnetization measurements indicate that both the materials show metallic behaviors and Pauli paramagnetism without CDW and superconducting transitions down to 2 K. The discovery of new V-based kagome metals proves that the kagome lattices of transition metals can be incorporated into more complicated structures. The structural flexibility of V-based kagome metals provides a new platform to study the possible correlated topological phenomena in this kind of materials.

References

[1] Balents L 2010 *Nature* **464** 199
[2] Han T H, Helton J S, Chu S, Nocera D G, Rodriguez-Rivera J A, Broholm C and Lee Y S 2012 *Nature* **492** 406
[3] Ye L, Kang M, Liu J, von Cube F, Wicker C R, Suzuki T, Jozwiak C, Bostwick A, Rotenberg E, Bell D C, Fu L, Comin R and Checkelsky J G 2018 *Nature* **555** 638
[4] Liu Z, Li M, Wang Q, Wang G, Wen C, Jiang K, Lu X, Yan S, Huang Y, Shen D, Yin J X, Wang Z, Yin Z, Lei H and Wang S 2020 *Nat. Commun.* **11** 4002
[5] Lin Z, Choi J H, Zhang Q, Qin W, Yi S, Wang P, Li L, Wang Y, Zhang H, Sun Z, Wei L, Zhang S, Guo T, Lu Q, Cho J H, Zeng C and Zhang Z 2018 *Phys. Rev. Lett.* **121** 096401
[6] Kang M, Ye L, Fang S, You J S, Levitan A, Han M, Facio J I, Jozwiak C, Bostwick A, Rotenberg E, Chan M K, McDonald R D, Graf D, Kaznatcheev K, Vescovo E, Bell D C, Kaxiras E, van den Brink J, Richter M, Ghimire M P, Checkelsky J G and Comin R 2020 *Nat. Mater.* **19** 163
[7] Liu E, Sun Y, Kumar N, Muechler L, Sun A, Jiao L, Yang S Y, Liu D, Liang A, Xu Q, Kroder J, Süß V, Borrmann H, Shekhar C, Wang Z, Xi C, Wang W, Schnelle W, Wirth S, Chen Y, Goennenwein S T B and Felser C 2018 *Nat. Phys.* **14** 1125
[8] Wang Q, Xu Y, Lou R, Liu Z, Li M, Huang Y, Shen D, Weng H, Wang S and Lei H 2018 *Nat. Commun.* **9** 3681
[9] Nakatsuji S, Kiyohara N and Higo T 2015 *Nature* **527** 212
[10] Yin J X, Zhang S S, Chang G, Wang Q, Tsirkin S S, Guguchia Z, Lian B, Zhou H, Jiang K, Belopolski I, Shumiya N, Multer D, Litskevich M, Cochran T A, Lin H, Wang Z, Neupert T, Jia S, Lei H and Hasan M Z 2019 *Nat. Phys.* **15** 443
[11] Yin J X, Zhang S S, Li H, Jiang K, Chang G, Zhang B, Lian B, Xiang C, Belopolski I, Zheng H, Cochran T A, Xu S Y, Bian G, Liu K, Chang T R, Lin H, Lu Z Y, Wang Z, Jia S, Wang W and Hasan M Z 2018 *Nature* **562** 91
[12] Yin J X, Ma W, Cochran T A, Xu X, Zhang S S, Tien H J, Shumiya N, Cheng G, Jiang K, Lian B, Song Z, Chang G, Belopolski I, Multer D, Litskevich M, Cheng Z J, Yang X P, Swidler B, Zhou H, Lin H, Neupert T, Wang Z, Yao N, Chang T R, Jia S and Hasan M Z 2020 *Nature* **583** 533
[13] Ortiz B R, Gomes L C, Morey J R, Winiarski M, Bordelon M, Mangum J S, Oswald I W H, Rodriguez-Rivera J A, Neilson J R, Wilson S D, Ertekin E, McQueen T M and Toberer E S 2019 *Phys. Rev. Mater.* **3** 094407
[14] Ortiz B R, Teicher S M L, Hu Y, Zuo J L, Sarte P M, Schueller E C, Abeykoon A M M, Krogstad M J, Rosenkranz S, Osborn R, Seshadri R, Balents L, He J and Wilson S D 2020 *Phys. Rev. Lett.* **125** 247002
[15] Ortiz B R, Sarte P M, Kenney E, Graf M J, Teicher S M L, Seshadri R and Wilson S D 2021 *Phys. Rev. Mater.* **5** 034801
[16] Yin Q, Tu Z, Gong C, Fu Y, Yan S and Lei H 2021 *Chin. Phys. Lett.* **38** 037403
[17] Yu S L and Li J X 2012 *Phys. Rev. B* **85** 144402
[18] Wang W S, Li Z Z, Xiang Y Y and Wang Q H 2013 *Phys. Rev. B* **87** 115135
[19] Kiesel M L, Platt C and Thomale R 2013 *Phys. Rev. Lett.* **110** 126405
[20] Liang Z, Hou X, Ma W, Zhang F, Wu P, Zhang Z, Yu F, Ying J J, Jiang K, Shan L, Wang Z and Chen X H 2021

Phys. Rev. X **11** 031026
[21] Li H X, Zhang T T, Pai Y Y, Marvinney C, Said A, Yilmaz T, Yin Q, Gong C, Tu Z, Vescovo E, Moore R G, Murakami S, Lei H C, Lee H N, Lawrie B and Miao H 2021 *Phys. Rev. X* **11** 031050
[22] Jiang Y X, Yin J X, Denner M M, Shumiya N, Ortiz B R, He J, Liu X, Zhang S S, Chang G, Belopolski I, Zhang Q, Hossain M S, Cochran T A, Multer D, Litskevich M, Cheng Z J, Yang X P, Guguchia Z, Xu G, Wang Z, Neupert T, Wilson S D and Hasan M Z 2021 *Nat. Mater.* **20** 1353
[23] Yang S Y, Wang Y, Ortiz B R, Liu D, Gayles J, Derunova E, Gonzalez-Hernandez R, Šmejkal L, Chen Y, Parkin S S P, Wilson S D, Toberer E S, McQueen T and Ali M N 2020 *Sci. Adv.* **6** abb6003
[24] Yu F H, Wu T, Wang Z Y, Lei B, Zhuo W Z, Ying J J and Chen X H 2021 *Phys. Rev. B* **104** L041103
[25] Feng X, Jiang K, Wang Z and Hu J 2021 *Sci. Bull.* **66** 1384
[26] Chen K Y, Wang N N, Yin Q W, Tu Z J, Gong C S, Sun J P, Lei H C, Uwatoko Y and Cheng J G 2021 *Phys. Rev. Lett.* **126** 247001
[27] Yu F H, Ma D H, Zhuo W Z, Liu S Q, Wen X K, Lei B, Ying J J and Chen X H 2021 *Nat. Commun.* **12** 3645
[28] Chen X, Zhan X, Wang X, Deng J, Liu X B, Chen X, Guo J G and Chen X 2021 *Chin. Phys. Lett.* **38** 057402
[29] Zhao C C, Wang L S, Xia W, Yin Q W, Ni J M, Huang Y Y, Tu C P, Tao Z C, Tu Z J, Gong C S, Lei H C, Guo Y F, Yang X F and Li S Y 2021 arXiv:2102.08356 [cond-mat.supr-con]
[30] Du F, Luo S, Ortiz B R, Chen Y, Duan W, Zhang D, Lu X, Wilson S D, Song Y and Yuan H 2021 *Phys. Rev. B* **103** L1220504
[31] Chen H, Yang H, Hu B, Zhao Z, Yuan J, Xing Y, Qian G, Huang Z, Li G, Ye Y, Yin Q, Gong C, Tu Z, Lei H, Ma S, Zhang H, Ni S, Tan H, Shen C, Dong X, Yan B, Wang Z and Gao H J 2021 *Nature* (to be published)
[32] APEX3 Ver. 2015 Bruker AXS, Inc., Madison, WI
[33] Sheldrick G M 2008 *Acta Crystal. Sec. A* **64** 112
[34] Wang Q, Sun S, Zhang X, Pang F and Lei H 2016 *Phys. Rev. B* **94** 075135
[35] Xiang Y, Li Q, Li Y, Xie W, Yang H, Wang Z, Yao Y and Wen H H 2021 arXiv:2104.06909 [cond-mat.supr-con]
[36] Ali M N, Xiong J, Flynn S, Tao J, Gibson Q D, Schoop L M, Liang T, Haldolaarachchige N, Hirschberger M, Ong N P and Cava R J 2014 *Nature* **514** 205
[37] Sun S, Wang Q, Guo P J, Liu K and Lei H 2016 *New J. Phys.* **18** 082002
[38] Pippard A B 1989 *Magnetoresistance in Metals* (Cambridge: University Press Cambridge)
[39] Ziman J M 1960 *Electrons and Phonons* (New York: Oxford University Press)